ARTICLE   OPEN

Check for updates

Madden-Julian oscillation influences United States springtime tornado and hail frequency

Douglas E. Miller [1✉], Vittorio A. Gensini [1] and Bradford S. Barrett [2]

The Madden–Julian Oscillation (MJO) is the dominant mode of intraseasonal variability in the tropics and has a documented influence on extratropical extreme weather through modulation of synoptic atmospheric conditions. MJO phase has been correlated with anomalous tornado and severe hail frequency in the United States (US). However, the robustness of this relationship is unsettled, and the variability of physical pathways to modulation is poorly understood, despite the socioeconomic impacts that tornadoes and hail evoke. We approached this problem using pentad MJO indices and practically perfect severe weather hindcasts. MJO lifecycles were cataloged and clustered to document variability and potential pathways to enhanced subseasonal tornado and hail predictability. Statistically significant increases in US tornado and hail probabilities were documented 3–4 weeks following the period of the strongest upper-level divergence for the 53 active MJO events that propagated past the Maritime continent, contrasting with the 47 MJO events that experienced the barrier effect, during boreal spring 1979–2019. The 53 MJO events that propagated past the Maritime continent revealed three prevailing MJO evolutions—each containing unique pathways and modulation of US tornado and hail frequency—advancing our knowledge and capability to anticipate these hazards at extended lead times.

INTRODUCTION

The Madden–Julian Oscillation[1] (MJO) has recently been exploited as a source of skillful subseasonal predictability for United States (US) severe convective storms (SCSs; tornadoes, severe hail, and damaging convective wind gusts)[2–4]. SCSs are a perennial source of insured losses totaling $10B annually[5] in the US, and their extended-range prediction remains an area of significant stakeholder interest[6]. The MJO is characterized as a meso-*a* cluster of deep convection in the Indian Ocean that migrates eastward into the Indo-Pacific warm pool with a timescale between 30 and 90 days[7,8]. Diabatic latent heating associated with extensive MJO convection can generate Rossby waves[9–14], as the divergent tropopause-level flow advects potential vorticity poleward and interacts with mid-latitude westerly jets[15–17]. MJO-induced wave trains often propagate poleward and eastward toward North America, altering the atmospheric circulation and associated probability and frequency of extreme temperatures and precipitation[18–23], atmospheric rivers[24,25], snowstorms[26,27], hurricanes[28,29], and SCSs[30–33]. In short, increasing our understanding of the MJO's influence and variability on extratropical extreme weather is vital to enhancing skillful subseasonal forecasts[34].

The MJO can be objectively characterized using a myriad of instantaneous or time-filtered tropical kinematic and thermodynamic quantities. The Real-time Multivariate MJO[35] (RMM) index uses meridional averages of outgoing longwave radiation (OLR)—along with 850-hPa and 200-hPa tropical zonal winds—to classify the MJO into one of eight phases and determine relative strength. The OLR-based MJO index[36] (OMI) aims to capture deep convection, derived by projecting 20–96 day filtered OLR anomalies onto the two leading spatial EOF patterns. Previous studies investigated the relationships between these MJO indices and US tornado and hail occurrence. For example, April tornado days were more likely during MJO RMM phases 6 and 8, whereas

May tornado days were more likely during MJO RMM phases 5 and 8[30]. Violent tornado outbreaks in the boreal spring were more than twice as likely during MJO RMM phase 2[31]. A comprehensive analysis examining OMI and RMM noted enhanced frequency of tornado days during phase 2 of the RMM, whereas OMI produced non-statistically significant results, highlighting the sensitivity of methods[37]. Strong instantaneous correlations between days with anomalous hail frequency and RMM MJO phase have also been noted[32].

In addition, the MJO has recently been leveraged to highlight potential SCS "forecasts of opportunity"[2,3]. Specifically, a statistically significant increase in central Great Plains tornado and hail frequency was evident 3–4 weeks following MJO OMI phase 8 and several weeks following phases 1 and 2[2]. A research team used the MJO in a pseudo-operational setting during April–May 2019 to anticipate an above-average tornado-frequency period 3–4 weeks in advance, which verified with tornado counts more than triple the expected 30-year average[4]. The onset of the significant MJO event was immediately followed by a period of above-average Earth-relative atmospheric angular momentum (AAM), subsequent breakdown of a strong zonally oriented north-Pacific jet stream, retrogression of the Rossby wave pattern over the conterminous US, and a favorable synoptic-scale atmospheric regime for SCSs[3,38].

Many studies examined the concurrent relationship between MJO phase and SCS frequency, but have omitted physical characteristics (e.g., strength, propagation speed) of individual MJO events that may have varied time-lagged responses. Here, we examine the MJO–SCS connection in the context of MJO lifecycle components and show significant modulations of tornado and hail probabilities following the period of the strongest MJO upper-level divergence. We show distinct pathways to SCS environment and event modulation that are *dependent on MJO flavor* (i.e.,

[1]Department of Geographic and Atmospheric Sciences, Northern Illinois University, DeKalb, IL, USA. [2]Air Force Office of Scientific Research, Santiago, Chile. ✉email: dmiller23@niu.edu
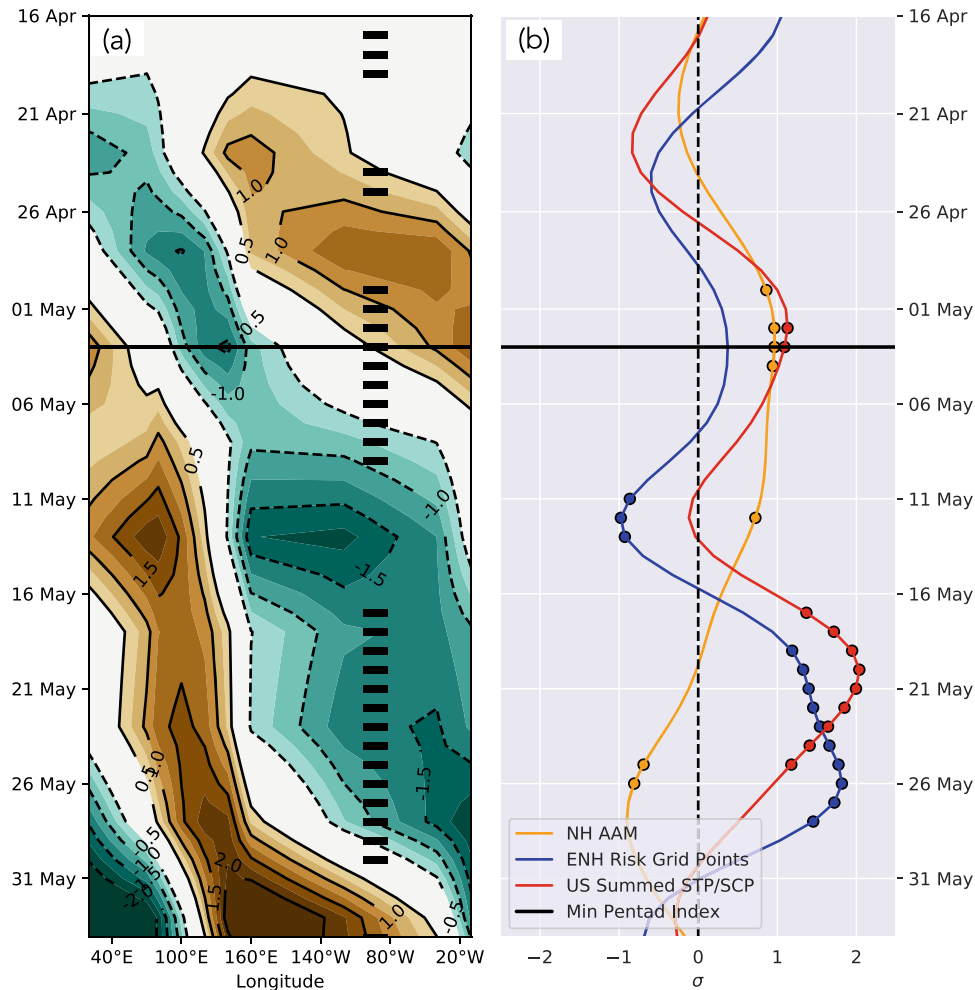
D.E. Miller et al.

Fig. 1 MJO pentad indices, Northern Hemisphere AAM, and tornado/hail modulation during 2019. a Hovmöller diagram of the 10 pentad MJO indices for April–May 2019 (shading) and marked occurrences of US practically perfect enhanced risk days (black bars). Green (brown) shading of the negative (positive) pentad indices represents 200-hPa divergence (convergence). Panel (**b**) indicates the standardized anomalies of northern hemisphere AAM (orange), number of practically perfect enhanced risk (PPH TOR >10% and/or PPH HAIL >30%) grid points (blue), and US accumulated sum of STP + SCP (red). Circles indicate significant anomalies using a 1000-iteration bootstrap test. Black horizontal line indicates the date of the first minimum pentad index, i.e., maximum upper-level divergence.

location, strength, and propagation speed). This work significantly advances our understanding of the boreal spring MJO–SCS relationship in the US, which is vital for improved subseasonal forecasts.

RESULTS AND DISCUSSION
An example of the MJO–SCS relationship during April–May 2019
We begin by presenting an example of a strong MJO event during April–May 2019, which resulted in a skillful subseasonal forecast of above-average US SCS frequency[3] (Fig. 1). The MJO event began in late April and continued to strengthen/propagate across the western Pacific through mid-May. This was reflected by periods of negative pentad anomalies (negative velocity potential at 200 hPa; $\chi 200$), indicative of upper-level divergence associated with deep convection. The 3–4 week period following the peak divergence during the MJO initiation recorded 14 days with tornado and hail practically perfect hindcast (PPH) risk at enhanced or greater levels across the US (Fig. 1a).

Northern Hemisphere AAM peaked near $+1\sigma$ on 3 May 2019, coinciding with the day of the minimum MJO pentad index, or maximum upper-level divergence (3 May 2019), and decreased

over the next four weeks (Fig. 1b). Such AAM increases are a response (via conservation of angular momentum) to poleward momentum flux from the tropics associated with the MJO convection[39]. Statistically significant peaks in PPH-enhanced risk grid points and summed Significant Tornado Parameter (STP) and Supercell Composite Parameter (SCP) were evident following the maximum-to-minimum transition of AAM through 31 May 2019 (Fig. 1b). Essentially, a favorable synoptic weather regime (western US upper-level thermal trough and downstream thermal ridge) remained in place from 17 to 28 May 2019[3], which increased the likelihood of positive PPH anomalies.

Modulation of hail and tornado frequency following minimum pentad index
High-frequency periods of SCSs following strong MJO events—like that observed during 2019—are evident from year-to-year. We examined each active MJO event during MAMJ from 1979 to 2019 along with its influence on tornado and hail PPH and the background convective environment (i.e., SCP and STP). An active MJO is identified if the minimum pentad index was ≤−0.5. Date and location of the minimum pentad indices for each active MJO event were cataloged, representing the point of minimum $\chi 200$ (or maximum 200-hPa divergence). This minimum is our proxy for
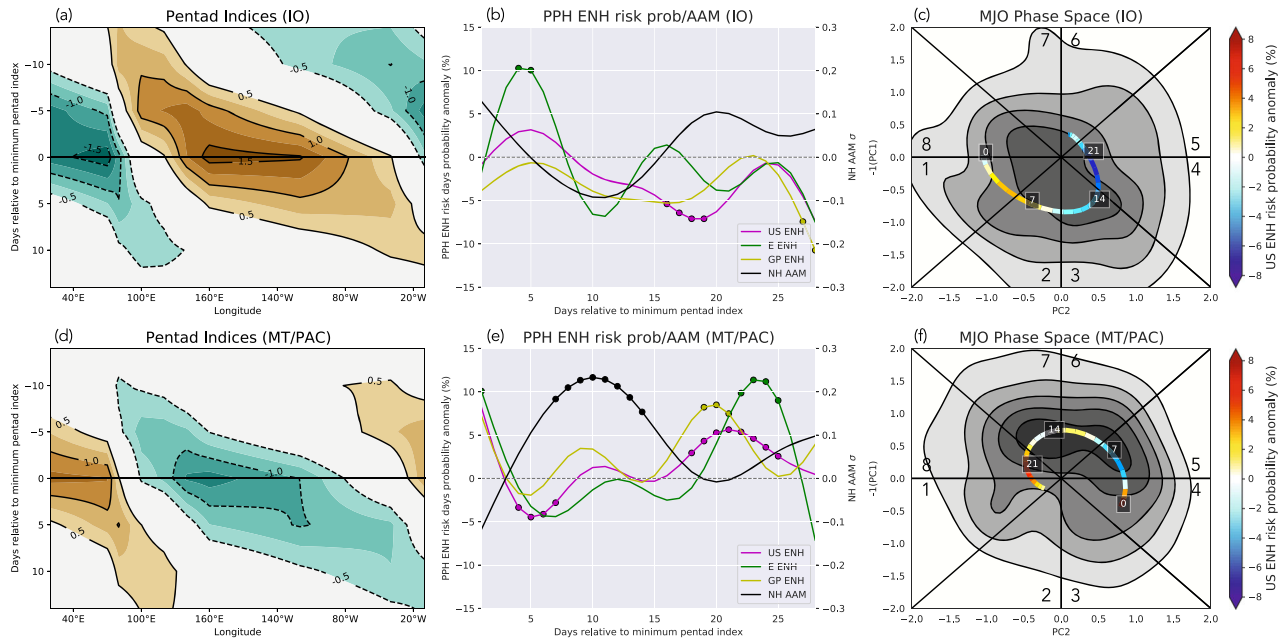
Fig. 2 IO and MT/PAC MJO pentad evolution and the resulting PPH modulation. a Hovmöller diagram of the 10 pentad MJO indices for 14 days prior to 14 days after the day of minimum pentad index for IO MJO events. Green (brown) shading of the negative (positive) pentad indices represents 200-hPa divergence (convergence). **b** Enhanced risk-day probability anomalies (%) for the US (pink), eastern US (green), and Great Plains (yellow), and standardized northern hemisphere AAM anomalies (black) following the date of minimum pentad index for IO MJO events. Statistically significant anomalies (bootstrapped p-values < 0.05) are shown by colored circles. **c** OMI phase-space kernel-density estimates (gray shading/contours, 0.03–0.21 every 0.03) and the mean event path of evolution from day 0 to 28 following the day of minimum pentad index for IO MJO events. Color shading represents US-enhanced risk-probability anomalies (%, pink curve in panel [**b**]). White numbers list the days following the minimum pentad index. Panels (**d**–**f**) as in (**a**–**c**), but for MT/PAC MJO events.

the peak lifecycle strength of MJO convection. To examine modulation of SCS frequency following MJO events, we composited probability anomalies of PPH-enhanced risk (TOR PPH ≥10% and/or HAIL PPH ≥30%) occurrence within a centered 3-day window for 28 days following the day of minimum pentad index (Fig. 2). One hundred active MJO events were recorded, which were further separated into two groups: 53 events that propagated across the Maritime Continent (MC) and 47 events that did not (i.e., which remained in the Indian Ocean, IO). The IO MJO composites were characterized by an ongoing MJO event that became active near the dateline and the minimum pentad indices occurred at 60°E, with conclusion of the events within the next 12 days (Fig. 2a). Statistically significant increases in the probability of eastern US (E) PPH-enhanced risk days peaked at days 4–5 following the minimum pentad index, with subsequent decreases in US probabilities noted at days 17–19 (Fig. 2b). IO MJO events progressed from OMI phase 8/1 on the day of minimum pentad index through phase 6 28 days later (Fig. 2c). This contrasts with previous research[2] that noted an increase in Great Plains tornado occurrence 3–4 weeks after OMI phase 8. However, these results are only valid for MJO events that reach peak amplitude in the IO and experience the MC barrier effect[40]. Phase-space diagrams involving the RMM[35] index were similar to the OMI phase-space diagrams throughout this study.

On average, the 53 MJO events that propagated past the Maritime Continent and into the Pacific (MT/PAC) strengthened while traveling through the Indo-Pacific warm pool (Fig. 2d). OMI phase space progressed through phases 4–1 for these events (Fig. 2f). Statistically significant increases in Northern Hemisphere AAM occurred at days 6–14 following the minimum pentad index, which coincided with a statistically significant decrease in the probability of US PPH-enhanced risk days, followed by statistically significant increases in Great Plains (GP) probabilities at days 19–21 and eastern US probabilities at days 22–25 (Fig. 2e).

Although the focus here is PPH-enhanced risks, similar modulations occurred for the probability of PPH moderate-risk days (TOR PPH ≥30% and/or HAIL PPH ≥60%; Supplementary Fig. 1).

We continue focus on the MT/PAC MJO events, as these were associated with a more robust modulation of tornado and hail frequency than the IO events. Perhaps most importantly, MT/PAC MJO events serve as potential forecasts of opportunity, given the temporal evolution of SCS probabilities. Composite anomalies of 3-day-averaged 500-hPa geopotential height (Z500), 3-day sums of accumulated STP and SCP, and the probability of PPH-enhanced risk occurrence within 3-day windows were examined (Fig. 3) to help physically explain the increased tornado and hail probabilities following the minimum pentad index in Fig. 2. A prominent Rossby wave train was present at day 14 following the minimum pentad index, spanning from the tropical–central Pacific to the western US, characterized by a statistically significant negative Z500 anomaly centered over the central Pacific (Fig. 3d). This pattern was also present at day 7 (although not as organized as day 14, Fig. 3a), with positive Z500 anomalies over the eastern US that persisted to day 14. The western US negative Z500 anomalies at day 14 transitioned through the central US at day 21, where statistically significant increases in STP and SCP and the probability of enhanced risk days rose over the southern Great Plains and southeast US (Fig. 3 h, i). Appreciable increases in the probability of PPH-enhanced risk days were greater when examining only strong MJO events (pentad index amplitude ≥1.0; Supplementary Fig. 2c), with a composite Z500 cyclone centered over Oklahoma and increased probabilities to the lee of the Z500 thermal trough axis in the expected surface cyclone "warm sector". The Z500 thermal trough migrated further east through day 28—decreasing PPH probabilities over the eastern US relative to day 21—as differential cold-air and anticyclonic vorticity advection forced subsidence, offshore surface winds,
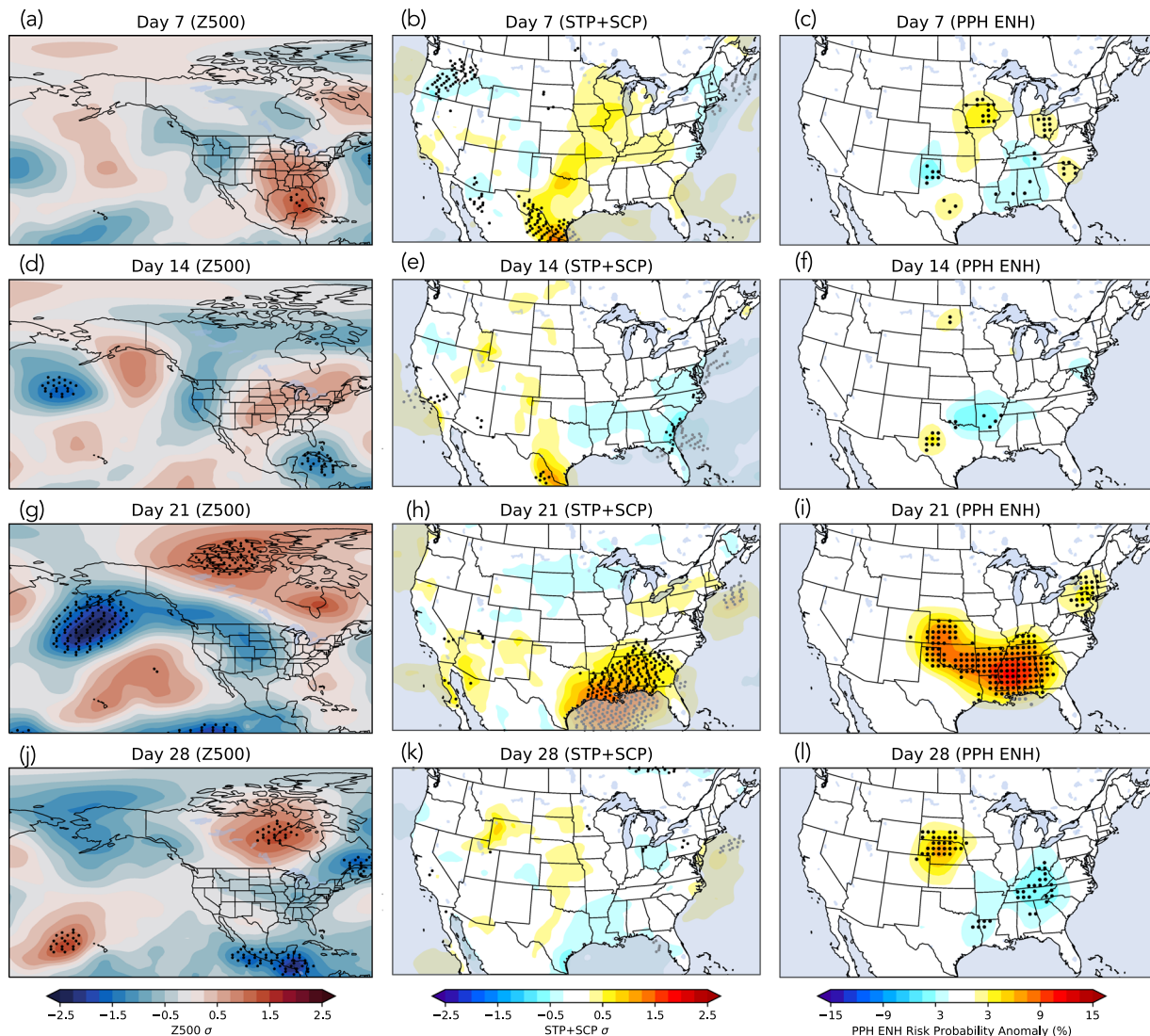
Fig. 3 Composite anomalies following day of minimum pentad index for MT/PAC MJO events. Three-day averaged Z500 standardized anomalies centered on (**a**) day 7, (**d**) day 14, (**g**) day 21, and (**j**) day 28 following the minimum pentad index day. Panels (**b**, **e**, **h**, **k**) follow (**a**, **d**, **g**, **j**), but for standardized anomalies of STP and SCP (shading). Panels (**c**, **f**, **i**, **l**) follow (**a**, **d**, **g**, **j**), but for anomalies of enhanced risk-day probability (%, shading). Black dots represent statistically significant anomalies at the 95% confidence level.

and unfavorable conditions for SCSs (Fig. 3j–l). The total evolution can be seen in Supplementary Movie 1.

Different MJO flavors influence hail and tornado probabilities

MJO events differ by strength and propagation speed[41–45], which can lead to modulation of the US synoptic weather pattern through different pathways[46]. To investigate this diversity, the 53 MT/PAC events were decomposed into three distinct MJO pentad evolutions. The weak (−1.0 < pentad indices ≤ −0.5) MJO events were labeled as cluster 1 (13 events), while clusters 2 and 3 were derived from k-means clustering containing 18 (cluster 2) and 22 (cluster 3) MJO events, respectively. Cluster-1 (Fig. 4a) MJO events represented shorter, weaker MJO events compared with clusters 2 and 3, as the cluster-1 composite showed an active, albeit weak MJO (pentad index amplitude <1) from day −3 to day +10. OMI phase space associated with cluster-1 events also displayed weak MJO events as noted by total amplitude values <1 (Fig. 4c). Cluster-2 events portrayed an ongoing MJO, with the greatest magnitudes of negative MJO pentad indices located between 160° E and 80°W. This cluster is representative of a quickly propagating

MJO (≈21°lon/day), as pentad indices ≤ −1 extended to the prime meridian by day +8 (Fig. 4d). On average, cluster-2 OMI phase space spanned from phase 4 to phase 2 over the 28-day period (Fig. 4f). Cluster-3 events were characterized by an active MJO similar to cluster-2 events (Fig. 4g). However, the largest magnitudes of these events were confined between 120°E and 140°E, and propagation was slower than cluster-2 (≈13.5°lon/day), with the maximum convection reaching 240°E eight days following the minimum pentad index. Cluster-3 OMI phase space indicated an active MJO starting in phase 3 at day 0 and progressed to phase 8 by day 28 (Fig. 4i).

To showcase the impacts of different MJO clusters on SCS frequency, we composited probability anomalies of PPH enhanced risk day occurrence and AAM for 28 days following the day of minimum pentad index (following the method of Fig. 2). Weaker MJO events (cluster 1) had no significant impact on AAM (on average) following the minimum pentad index, or maximum upper-level divergence, until day 20, which then coincided with a statistically significant increase in the probability of US PPH ENH risks from days 22 to 28 (Fig. 4b). This increase is attributed to a substantial western US Z500 anticyclone evident at day 14 (a
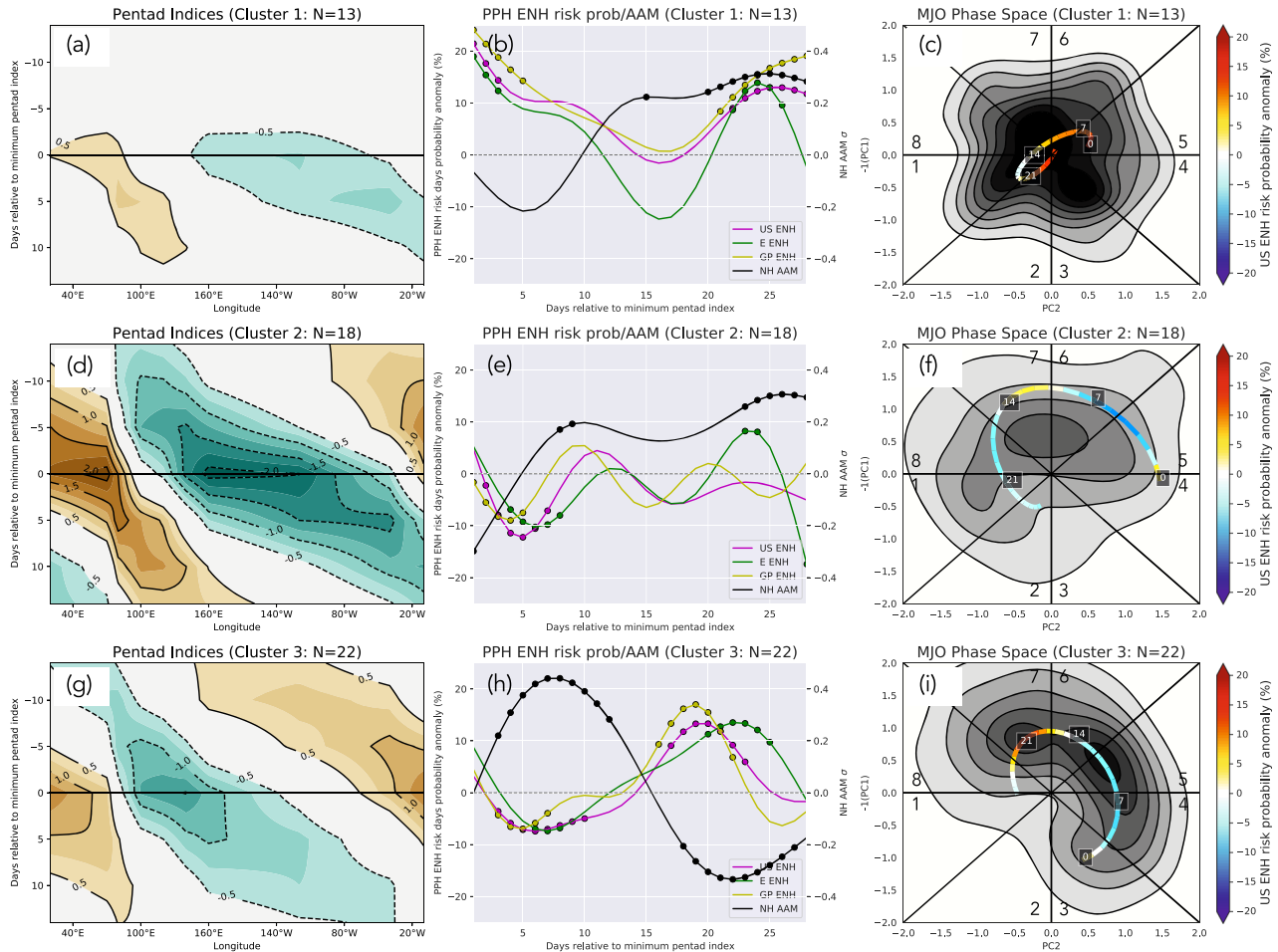
Fig. 4 MJO pentad evolution and the resulting PPH modulation for the three clusters of MT/PAC events. Panels (**a**, **b**, **c**) as Fig. 2, but for cluster-1 MJO events. Panels (**d**, **e**, **f**) as panels (**a**, **b**, **c**) but for cluster-2 MJO events. Panels (**g**, **h**, **i**) as panels (**a**, **b**, **c**) but for cluster-3 MJO events.

pattern which is unfavorable for widespread SCS activity) that migrated northeast into eastern Canada by day 21 (Supplementary Fig. 3d, g). The western US trough–eastern US ridge pattern, supporting southerly surface flow from the Gulf of Mexico, increased the probability of SCS occurrence throughout the Great Plains (Supplementary Fig. 3g) at day 21 following the minimum pentad index for cluster-1 events. Cluster-2 MJO events experienced statistically significant increases in the probability of ENH risk occurrence over the eastern US at days 23–24 following the minimum pentad index (Fig. 4e). A composite Z500 anticyclone was present over the western US with eastern US troughing at day 21, and increased probabilities of PPH were noted over the southeast US just east of the 500-hPa thermal trough axis (Supplementary Fig. 3h). MJO events associated with cluster-3 exhibited significant increases in AAM during days 3–12 following the minimum pentad index, and increases in the probability of ENH risk days were evident days 16–22 for the GP and days 20–25 for the eastern US (Fig. 4h). A composite eastern US Z500 thermal ridge was evident at day 14, with increased SCS probabilities throughout the Great Plains (Supplementary Fig. 3f). In fact, the anticyclone first developed around day 10 and persisted over the eastern US, until migrating southeast into day 21 (Supplementary Movie 2). The most robust signal was derived at day 21, with a composite anticyclone centered over south Florida with a SW-to-NE tilt. Onshore surface flow associated with the anticyclonic

circulation supported increased probabilities of SCS frequency focused on the Ark-La-Tex region (Supplementary Fig. 3i).

Implications for monitoring and prediction

Our results highlight increased understanding of MJO-induced variability associated with US springtime tornado and hail events, which is important for their subseasonal prediction. The timing of peak tornado and hail-frequency anomalies was unique and dependent on MJO type, strength, and propagation speed. Few statistically significant increases in the probability of US PPH ENH risk days occurred following MJO events that experienced the barrier effect (IO), while weak MT/PAC events (cluster 1) experienced increases in US PPH ENH risk probabilities during the week-4 period. The late March into early April 2011 MJO event (and associated high tornado and hail-frequency period of mid-to-late April 2011[47]) was classified as cluster 3 (Supplementary Fig. 4), characteristic of increased ENH risk probabilities during weeks 3–4 following the minimum pentad index. The previously discussed high-frequency tornado and hail period of late May 2019[3] was also labeled cluster 3. In that event, the minimum pentad index occurred on 3 May 2019. By 20 May, a quasi-stationary western US mid-level thermal trough was established (similar to patterns in Supplementary Fig. 3), which helped force favorable synoptic-scale conditions for hailstorms and tornadoes.

The main caveat associated with our (and other similar) analysis is sample size. We are limited by the number of years in the study

and the temporal frequency at which MJO events cycle in the boreal spring (e.g., if MJO events were examined over thousands of years, it would be likely that more than three clusters would emerge). Future work may focus on the issue of sample size by utilizing climate-model simulations, allowing for more robust results and avenues to explore the impacts of additional modes of climate variability on the MJO and SCS occurrence. Nevertheless, our work highlights pathways forward for better prediction and understanding of how the MJO clusters influence US tornado and hail frequency. This could be especially beneficial for subseasonal SCS forecasts that utilize a hybrid dynamical/statistical approach[48], as such forecasts could be probability-weighted by observed MJO characteristics.

METHODS

MJO indices

Pentad MJO indices were obtained from the NOAA Climate Prediction Center and represent the negative projection of 200-hPa velocity-potential (χ200) anomalies onto the ten time-lagged patterns of the first extended empirical orthogonal function (EEOF) of pentad χ200 anomalies[49,50]. Pentad indices are available at 20°E, 70°E, 80°E, 100°E, 120°E, 140°E, 160°E, 120°W, 40°W, and 10°W, and can be viewed graphically to examine evolution of enhanced and suppressed tropical 200-hPa divergence (e.g., Fig. 1). We identified active MJO events from 1979 to 2019 using pentad indices during the extended boreal spring season (MAMJ), as this corresponds to the annual climatological peak in tornado and hail frequency[51,52]. An active MJO event was defined where pentad indices were ≤–0.5. Date and location of the minimum pentad indices for each MJO event were cataloged, representing the spatiotemporal maximum 200-hPa divergence, or maximum convection, for each event. The minimum pentad index must be at or west of 160°E. MJO events were classified by the barrier effect[40] (i.e., propagated across the Maritime Continent or not). For robustness, we also compared MJO pentad indices to the OLR-based MJO index[36] (OMI). OMI phase spaces are shown in Figs. 2 and 4.

Tornado and hail data

Tornado and hail practically perfect hindcasts (PPH)[53,54] were used as a "target" for the MJO pentad data. PPH represents a Gaussian-smoothed statistical point process of event probabilities based on observed tornado and hail reports. PPH probabilities were constructed to resemble what a perfect Storm Prediction Center (SPC) SCS outlook may have looked like. PPH data were calculated on the National Center for Environmental Predictions's 211 Lambert-conformal grid (≈80-km horizontal grid spacing) following previous work[54]. The probability of a PPH "enhanced; ENH" (tornado PPH ≥10% and/or hail PPH ≥30%) day centered within a 3-day window was calculated for the US, defined as all US grid points east of 106° W. Two additional regions were analyzed: the Great Plains (GP: 106–91°W) and the eastern US (E: east of 91°W). We also examined PPH "moderate; MDT" (tornado PPH ≥30% and/or hail PPH ≥60%) risk days. After calculating the probability of PPH ENH risk occurrence, the climatological probabilities were removed in Figs. 2 and 4. The climatology was calculated as the probability of a PPH risk day to occur within a 3-day window during the 28 days following the minimum pentad index over the 41-year period (1979–2019). For example, the climatological probability was calculated each day over the 28-day period 3–31 May 1979–2019, when examining the 3 May 2019 MJO event.

Reanalyses

To supplement PPH observations, atmospheric conditions conducive for tornadoes and hail were assessed from the North American Regional Reanalysis (NARR)[55]. The significant tornado parameter (STP) and supercell composite parameter (SCP) were calculated[56] using 3-hourly NARR fields and summed from 1200 to 1200 UTC (following previous work[57,58]) to capture the typical diurnal cycle of SCS frequency. NARR was selected due to its documented ability to adequately represent important atmospheric ingredients related to SCSs[59,60].

To highlight planetary and synoptic-scale features, 1200–1200 UTC daily averaged (from the native hourly interval) 500-hPa geopotential height

(Z500) was obtained from the ECMWF ERA5 reanalysis[61]. Standardized anomalies were calculated using the 1979–2019 climatology.

Earth-relative atmospheric angular momentum (AAM) was calculated, given its documented relationship to MAMJ tornado and hail frequency in the US[38,62]. Daily (1200–1200 UTC) mean AAM values were calculated from 6-hourly intervals using zonal wind and surface pressure from ERA5's 137 native vertical hybrid-sigma levels[61]. Earth-relative AAM was derived following[63]:

$$AAM = \frac{a^3}{g} \int_{-\frac{\pi}{2}}^{\frac{\pi}{2}} \int_{0}^{2\pi} \int_{P_o}^{p} cos^2\phi d\phi d\lambda u dp \tag{1}$$

where a is Earth's radius, g is the gravitational constant, ϕ is latitude, λ is longitude, u is zonal wind speed, and p is pressure. Here, we limit the zonal integral to only the Northern Hemisphere (i.e., $0 \le \phi \le \frac{\pi}{2}$), given our interest on the impact of SCSs in the US.

Decomposition of MJO events

To separate the MJO events into subgroups, cluster 1 first contains the 13 weaker MJO events (–1.0 < minimum pentad index ≤–0.5). Clusters 2 and 3 are derived using k-means clustering following Lloyd's algorithm[64]. The algorithm was applied to the pentad MJO indices from 14 days prior to 14 days following the day of the minimum pentad index (i.e., maximum divergence).

Statistical significance

Composite evolutions of PPH-enhanced risk-day probabilities were constructed following minimum pentad indices. A 1000-iteration bootstrap test was performed to test the significance of the daily (1200–1200 UTC) anomalies of PPH probabilities following the minimum pentad index (Figs. 2 and 4). The significance of Z500 anomalies was tested using a two-tailed Student's t-test, with the null hypothesis that the anomalies do not differ from zero. A Mann–Whitney U-test for the medians was performed on the anomalies of STP/SCP and PPH as the distributions were non-Gaussian. The results were considered significant if the p-value was less than 0.05 (95% confidence level).

DATA AVAILABILITY

NARR reanalysis data are available through the NCAR Research Data Archive (RDA; https://rda.ucar.edu/). ERA5 data were downloaded from the European Centre for Medium-Range Weather Forecasts (ECMWF), Copernicus Climate Change Service (C3S) available at https://cds.climate.copernicus.eu/. The CPC Pentad MJO indices are available online at https://www.cpc.ncep.noaa.gov/products/precip/CWlink/daily_mjo_index/pentad.html. PPH data are available online at https://atlas.niu.edu/pperfect/BAMS/.

CODE AVAILABILITY

The source codes for the analysis of this study are available from the corresponding author upon reasonable request.

REFERENCES

1. Madden, R. A. & Julian, P. R. Detection of a 40–50 day oscillation in the zonal wind in the tropical Pacific. *J. Atmos. Sci.* **28**, 702–708 (1971).
2. Baggett, C. F. et al. Skillful subseasonal forecasts of weekly tornado and hail activity using the Madden-Julian oscillation. *J. Geophys. Res. Atmos.* **123**, 12–661 (2018).
3. Gensini, V. A., Gold, D., Allen, J. T. & Barrett, B. S. Extended US tornado outbreak during late May 2019: a forecast of opportunity. *Geophys. Res. Lett.* **46**, 10150–10158 (2019).
4. Gensini, V. A., Barrett, B. S., Allen, J. T., Gold, D. & Sirvatka, P. The extended-range tornado activity forecast (ERTAF) project. *Bull. Am. Meteorol. Soc.* **101**, E700–E709 (2020).
5. Smith, A. B. & Katz, R. W. Us billion-dollar weather and climate disasters: data sources, trends, accuracy and biases. *Nat. Hazards* **67**, 387–410 (2013).

6. Robertson, A. W., Camargo, S. J., Sobel, A., Vitart, F. & Wang, S. Summary of workshop on sub-seasonal to seasonal predictability of extreme weather and climate. *NPJ Clim. Atmos. Sci.* **1**, 20178 (2018).

7. Zhang, C. Madden-Julian oscillation. *Rev. Geophys.* https://doi.org/10.1029/2004RG000158 (2005).

8. Zhang, C. et al. Cracking the MJO nut. *Geophys. Res. Lett.* **40**, 1223–1230 (2013).

9. Hoskins, B. J. & Karoly, D. J. The steady linear response of a spherical atmosphere to thermal and orographic forcing. *J. Atmos. Sci.* **38**, 1179–1196 (1981).

10. Sardeshmukh, P. D. & Hoskins, B. J. The generation of global rotational flow by steady idealized tropical divergence. *J. Atmos. Sci.* **45**, 1228–1251 (1988).

11. Bladé, I. & Hartmann, D. L. The linear and nonlinear extratropical response of the atmosphere to tropical intraseasonal heating. *J. Atmos. Sci.* **52**, 4448–4471 (1995).

12. Jin, F. & Hoskins, B. J. The direct response to tropical heating in a baroclinic atmosphere. *J. Atmos. Sci.* **52**, 307–319 (1995).

13. Hendon, H. H. & Salby, M. L. Planetary-scale circulations forced by intraseasonal variations of observed convection. *J. Atmos. Sci.* **53**, 1751–1758 (1996).

14. Tseng, K.-C., Maloney, E. & Barnes, E. The consistency of MJO teleconnection patterns: an explanation using linear Rossby wave theory. *J. Clim.* **32**, 531–548 (2019).

15. Knutson, T. R. & Weickmann, K. M. 30–60 day atmospheric oscillations: composite life cycles of convection and circulation anomalies. *Mon. Wea. Rev.* **115**, 1407–1436 (1987).

16. Kiladis, G. N. & Weickmann, K. M. Circulation anomalies associated with tropical convection during northern winter. *Mon. Wea. Rev.* **120**, 1900–1923 (1992).

17. Stan, C. et al. Review of tropical-extratropical teleconnections on intraseasonal time scales. *Rev. Geophys.* **55**, 902–937 (2017).

18. Zhou, S., L'Heureux, M., Weaver, S. & Kumar, A. A composite study of the MJO influence on the surface air temperature and precipitation over the continental United States. *Clim. Dyn.* **38**, 1459–1471 (2012).

19. Schreck, C. J., Cordeira, J. M. & Margolin, D. Which MJO events affect North American temperatures? *Mon. Wea. Rev.* **141**, 3840–3850 (2013).

20. Lee, Y.-Y. & Grotjahn, R. Evidence of specific MJO phase occurrence with summertime California Central Valley extreme hot weather. *Adv. Atmos. Sci.* **36**, 589–602 (2019).

21. Jenney, A., Nardi, K., Barnes, E. & Randall, D. The seasonality and regionality of MJO impacts on North American temperature. *Geophysi. Res. Lett.* **46**, 9193–9202 (2019).

22. Arcodia, M. C., Kirtman, B. P. & Siqueira, L. S. How MJO teleconnections and ENSO interference impacts US precipitation. *J. Clim.* **33**, 4621–4640 (2020).

23. Nardi, K. M. et al. Skillful all-season S2S prediction of US precipitation using the MJO and QBO. *Weather Forecast.* **35**, 2179–2198 (2020).

24. Mundhenk, B. D., Barnes, E. A., Maloney, E. D. & Baggett, C. F. Skillful empirical subseasonal prediction of landfalling atmospheric river activity using the Madden–Julian oscillation and quasi-biennial oscillation. *npj Clim. Atmos. Sci.* **1**, 20177 (2018).

25. DeFlorio, M. J. et al. Experimental subseasonal-to-seasonal (S2S) forecasting of atmospheric rivers over the Western United States. *J. Geophys. Res. Atmos.* **124**, 11242–11265 (2019).

26. Moon, J.-Y., Wang, B. & Ha, K.-J. MJO modulation on 2009/10 winter snowstorms in the United States. *J. Clim.* **25**, 978–991 (2012).

27. Klotzbach, P. J., Oliver, E. C., Leeper, R. D. & Schreck III, C. J. The relationship between the Madden–Julian oscillation (MJO) and southeastern New England snowfall. *Mon. Wea. Rev.* **144**, 1355–1362 (2016).

28. Maloney, E. D. & Hartmann, D. L. Modulation of hurricane activity in the Gulf of Mexico by the Madden-Julian oscillation. *Science* **287**, 2002–2004 (2000).

29. Barrett, B. S. & Leslie, L. M. Links between tropical cyclone activity and Madden–Julian oscillation phase in the north Atlantic and northeast Pacific basins. *Mon. Wea. Rev.* **137**, 727–744 (2009).

30. Barrett, B. S. & Gensini, V. A. Variability of central United States April-May tornado day likelihood by phase of the Madden-Julian oscillation. *Geophys. Res. Lett.* **40**, 2790–2795 (2013).

31. Thompson, D. B. & Roundy, P. E. The relationship between the Madden–Julian oscillation and US violent tornado outbreaks in the spring. *Mon. Wea. Rev.* **141**, 2087–2095 (2013).

32. Barrett, B. S. & Henley, B. N. Intraseasonal variability of hail in the contiguous United States: relationship to the Madden–Julian oscillation. *Mon. Wea. Rev.* **143**, 1086–1103 (2015).

33. Moore, T. W. & McGuire, M. P. Tornado-days in the United States by phase of the Madden–Julian oscillation and global wind oscillation. *Clim. Dyn.* **54**, 17–36 (2020).

34. Vitart, F. & Robertson, A. W. The sub-seasonal to seasonal prediction project (S2S) and the prediction of extreme events. *NPJ Clim. Atmos. Sci.* **1**, 3 (2018).

35. Wheeler, M. C. & Hendon, H. H. An all-season real-time multivariate MJO index: development of an index for monitoring and prediction. *Mon. Wea. Rev.* **132**, 1917–1932 (2004).

36. Kiladis, G. N. et al. A comparison of OLR and circulation-based indices for tracking the MJO. *Mon. Wea. Rev.* **142**, 1697–1715 (2014).

37. Tippett, M. K. Robustness of relations between the MJO and US tornado occurrence. *Mon. Wea. Rev.* **146**, 3873–3884 (2018).

38. Gensini, V. A. & Marinaro, A. Tornado frequency in the United States related to global relative angular momentum. *Mon. Wea. Rev.* **144**, 801–810 (2016).

39. Weickmann, K. & Berry, E. A synoptic-dynamic model of subseasonal atmospheric variability. *Mon. Wea. Rev.* **135**, 449–474 (2007).

40. Zhang, C. & Ling, J. Barrier effect of the Indo-Pacific Maritime Continent on the MJO: perspectives from tracking MJO precipitation. *J. Clim.* **30**, 3439–3459 (2017).

41. Sobel, A. & Maloney, E. Moisture modes and the eastward propagation of the MJO. *J. Atmos. Sci.* **70**, 187–192 (2013).

42. Kim, H., Janiga, M. A. & Pegion, K. MJO propagation processes and mean biases in the SubX and S2S reforecasts. *J. Geophys. Res. Atmos.* **124**, 9314–9331 (2019).

43. Chen, G. & Wang, B. Circulation factors determining the propagation speed of the Madden–Julian oscillation. *J. Clim.* **33**, 3367–3380 (2020).

44. Wang, T. & Li, T. Factors controlling the diversities of MJO propagation and intensity. *J. Clim.* **34**, 6549–6563 (2021).

45. Barrett, B. S., Densmore, C. R., Ray, P. & Sanabia, E. R. Active and weakening MJO events in the maritime continent. *Clim. Dyn.* **57**, 157–172 (2021).

46. Zheng, C. & Chang, E. K. The role of MJO propagation, lifetime, and intensity on modulating the temporal evolution of the MJO extratropical response. *J. Geophys. Res. Atmos.* **124**, 5352–5378 (2019).

47. Knupp, K. R. et al. Meteorological overview of the devastating 27 April 2011 tornado outbreak. *Bull. Am. Meteorol. Soc.* **95**, 1041–1062 (2014).

48. Miller, D. E., Wang, Z., Trapp, R. J. & Harnos, D. S. Hybrid prediction of weekly tornado activity out to Week 3: Utilizing weather regimes. *Geophys. Res. Lett.* **47**, e2020GL087253 (2020).

49. CPC pentad MJO indices. https://www.cpc.ncep.noaa.gov/products/precip/CWlink/daily_mjo_index/pentad.html (2022).

50. Baxter, S., Weaver, S., Gottschalck, J. & Xue, Y. Pentad evolution of wintertime impacts of the Madden–Julian oscillation over the contiguous United States. *J. Clim.* **27**, 7356–7367 (2014).

51. Brooks, H. E., Doswell, C. A. & Kay, M. P. Climatological estimates of local daily tornado probability for the United States. *Wea. Forecast.* **18**, 626–640 (2003).

52. Cintineo, J. L., Smith, T. M., Lakshmanan, V., Brooks, H. E. & Ortega, K. L. An objective high-resolution hail climatology of the contiguous United States. *Wea. Forecast.* **27**, 1235–1248 (2012).

53. Hitchens, N. M., Brooks, H. E. & Kay, M. P. Objective limits on forecasting skill of rare events. *Wea. Forecast.* **28**, 525–534 (2013).

54. Gensini, V. A., Haberlie, A. M. & Marsh, P. T. Practically perfect hindcasts of severe convective storms. *Bull. Am. Meteorol. Soc.* **101**, E1259–E1278 (2020).

55. Mesinger, F. et al. North American regional reanalysis. *Bull. Am. Meteorol. Soc.* **87**, 343–360 (2006).

56. Thompson, R. L., Edwards, R., Hart, J. A., Elmore, K. L. & Markowski, P. Close proximity soundings within supercell environments obtained from the Rapid Update Cycle. *Wea. Forecast.* **18**, 1243–1261 (2003).

57. Gensini, V. A. & Bravo de Guenni, L. Environmental covariate representation of seasonal US tornado frequency. *J. Appl. Meteorol. Climatol.* **58**, 1353–1367 (2019).

58. Gensini, V. A. & Tippett, M. K. Global ensemble forecast system (GEFS) predictions of days 1–15 US tornado and hail frequencies. *Geophys. Res. Lett.* **46**, 2922–2930 (2019).

59. Gensini, V. A., Mote, T. L. & Brooks, H. E. Severe-thunderstorm reanalysis environments and collocated radiosonde observations. *J. Appl. Meteorol. Climatol.* **53**, 742–751 (2014).

60. King, A. T. & Kennedy, A. D. North American supercell environments in atmospheric reanalyses and RUC-2. *J. Appl. Meteorol. Climatol.* **58**, 71–92 (2019).

61. Hersbach, H. et al. The ERA5 global reanalysis. *Q. J. R. Meteorol. Soc.* **146**, 1999–2049 (2020).

62. Gensini, V. A. & Allen, J. T. US hail frequency and the global wind oscillation. *Geophys. Res. Lett.* **45**, 1611–1620 (2018).

63. Hide, R., Birch, N., Morrison, L., Shea, D. & White, A. Atmospheric angular momentum fluctuations and changes in the length of the day. *Nature* **286**, 114–117 (1980).

64. Lloyd, S. Least squares quantization in PCM. *IEEE Trans. Inf. Theory* **28**, 129–137 (1982).

ACKNOWLEDGEMENTS

AUTHOR CONTRIBUTIONS

V.G. and B.B. conceived the study. D.M. and V.G. designed the study. D.M. performed the analysis. D.M. led the figure creation with assistance from V.G. All authors aided in the interpretation of results. All authors contributed to editing, with D.M. and V.G. leading the initial draft.

COMPETING INTERESTS

The authors declare no competing interests.

ADDITIONAL INFORMATION

Supplementary information The online version contains supplementary material available at https://doi.org/10.1038/s41612-022-00263-5.

Correspondence and requests for materials should be addressed to Douglas E. Miller.

Reprints and permission information is available at http://www.nature.com/reprints